

Precision Measurement and Modeling of Quenching-Tempering Distortion in Low-Alloy Steel Components with Internal Threads

Zhenguo Nie, Gang Wang, Yongliang Lin, and Yiming (Kevin) Rong

(Submitted March 5, 2015; in revised form October 14, 2015; published online November 24, 2015)

Distortion resulting from heat treatment may cause serious problems for precision parts. A precision component made from 30CrNi3Mo steel with internal threads distorts slightly after quenching-tempering treatment. Such a small distortion results in serious difficulties in the subsequent assembly process. The distortion of the internal thread was measured using semi-destructive testing with video measuring system. Periodic wavy distortions emerged in the internal threads after heat treatment. Then both XRD analysis and hardness testing were conducted. A numerical simulation of the complete quenching-tempering process was conducted by DANTE, which is a set of user subroutines that link into the ABAQUS/STD solver. The results from the simulations are in good agreement with the measurement in distortion, microstructure field, and hardness. The effects of the technological parameters including quenchant, immersion orientation, and grooves were discussed on the basis of the simulation results. Finally, strategies to significantly decrease distortion and residual stress are proposed.

Keywords 30CrNi3Mo steel, distortion, internal thread, quenching-tempering

1. Introduction

Heat treatment processes have long been used to improve the mechanical properties of steel components. Today, performance control and shape control are two major targets faced by scientific researchers and industrial engineers. Distortion caused by phase transformations and thermal stress remains an important problem that hinders the production of precise components.

The distortion resulting from heat treatment was studied a lot by both experiments and finite element method. The FEA model can be used to acquire the distribution of the temperature and residual stress, which could be validated by previously reported experiments (Ref 1-5). The simulation results played an important role in designing new products and in optimizing the quenching process (Ref 6-9). Phase transformation is the main mechanism for distortion, and the extent of distortion can be decreased by controlling the cooling rate (Ref 10). Choosing a suitable quenchant is very important for controlling the

cooling rate (Ref 3). The sensitivity of the material properties to the distortion and residual stress during the metal quenching process was studied using FEA. It was found that thermal conductivity, martensitic start temperature, and shear modulus were the dominant material properties which strongly influenced the curvature and effective stress (Ref 11). The volume fraction of the microstructure could be predicted using the finite element method and finite volume method (Ref 12, 13). FEM modeling of quenching and tempering processes remains challenging due to tempering uncertainty. This uncertainty is predominantly caused by stress relaxation and microstructure evolution.

Measuring a tiny distortion inside a precise component with an internal thread after being subjected to a quenching-tempering process is quite a difficult problem, particularly when the component is very small because the optical probe cannot penetrate into the interior or the threaded hole. In addition, the tempering process cannot be ignored in a finite element analysis (FEA). The entire quenching and tempering process should be modeled to predict distortion and residual stress.

In this paper, the entire quenching-tempering process is investigated using experiments and simulations. A component made from 30CrNi3Mo steel with internal threads is quenched and tempered. The distortion of the internal threads is measured by semi-destructive testing using a video measuring system. Also, XRD analysis and hardness testing of the tempered material are performed. Then FEA of the heat treatment is conducted. The temperature field, stress field, microstructure field, and distortion are all obtained. The precision and accuracy of the model can be validated using the measured distortion, microstructure fields, and hardness results. In addition, the effects of parameters (tempering temperature and holding time) in the tempering process, different quenchants (UCON, water, and oil), immersion orientation, air transfer, and simulation without grooves are studied. Finally, several useful suggestions are proposed to the manufacturers based on the simulation results.

Zhenguo Nie and **Gang Wang**, Beijing Key Lab of Precision/Ultra-precision Manufacturing Equipments and Control, Department of Mechanical Engineering, Tsinghua University, Beijing, 100084, China; **Yongliang Lin**, School of Mechanical Electronic and Control Engineering, Beijing Jiaotong University, Beijing, 100044, China; and **Yiming (Kevin) Rong**, Beijing Key Lab of Precision/Ultra-precision Manufacturing Equipments and Control, Department of Mechanical Engineering, Tsinghua University, Beijing, 100084, China and Department of Mechanical Engineering, Worcester Polytechnic Institute, Worcester, MA, 01609, US. Contact e-mails: niezhenguo@126.com, nyzg12@mails.tsinghua.edu.cn, and gwang@tsinghua.edu.cn

2. Experimental Design and Precision Measurements

As shown in Fig. 1, the precision screw nut has internal threads inside with six grooves outside. The screw nut is used in the precision screw rod, and the accuracy should be very high for a fluent and stable motion. Even a small distortion may hamper the screw cap performance.

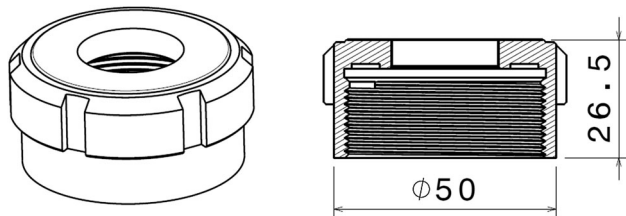


Fig. 1 Geometry of the component (units: mm)

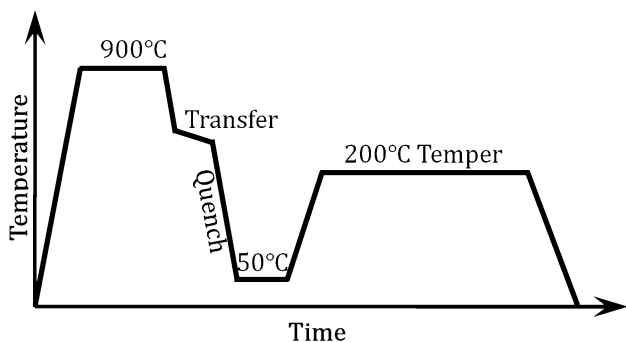
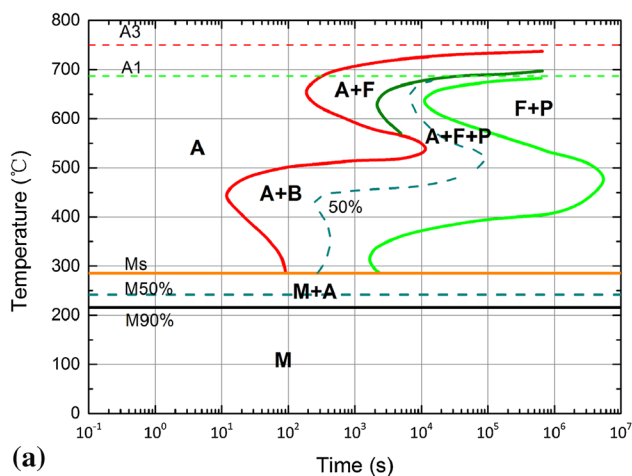


Fig. 2 Processing flow chart of heat treatment

Table 1 Chemical composition of 30CrNi3Mo steel (wt.%)

C	Si	Mn	Cr	Ni	Mo	Fe
0.32	0.21	0.65	1.42	2.86	0.30	Bal



2.1 Experimental Design

The processing conditions used are shown in Fig. 2. Before being quenched, the component is transferred through the air and then immersed into the quenchant. After the small end is immersed into quenchant, it is tempered at 200 °C for 1.5 h and then cooled to room temperature using air.

The component is made of 30CrNi3Mo steel, which is a medium-carbon low-alloy super-high-strength steel. Its chemical composition is shown in Table 1 as measured by EPMA. 30CrNi3Mo steel has good quenching properties and excellent mechanical properties. 30CrNi3Mo steel is usually used as an armor plate material to provide protection in military and non-military vehicles. This particular type of steel exhibits quite good hardenability due to its relatively high Ni content; thus, martensitic structures can be completely obtained in air-cooling conditions. Generally, quenching and tempering are well-established methods for strengthening steel due to the precipitation of fine and disperse alloy carbides during tempering (Ref 14). Its TTT and CCT diagrams are determined by experiment as shown in Fig. 3. In the simulation, the CCT diagram is used to obtain the parameters of transformation kinetics.

2.2 Precision Measurements of the Distortion

Video measuring system is adopted to obtain the shape change of thread (Fig. 4). The optical probe can be used to obtain the image of the object to be tested. With moving the object, the whole image is obtained. In this measurement, JVL250 video measuring system can reach a maximum of one micrometer.

Semi-destructive testing using a video measuring system was adopted to measure the distortion of the internal threads, as shown in Fig. 5. The semi-destructive nature of this characterization technique means that one-sixth of the component is cut off. However, the part is not cut off completely, and a bridge structure on the top is preserved to avoid distortion recovery. The optical probe can then obtain an image of the thread through this gap. The region within red rectangle is the field of view. The cross section of the thread is trapezoid shaped.

The thread boundary can be read point by point from the image, just as the line in Fig. 6. The bright part is the crest, and the dim part is the root. The crest can reflect more light than the root. The entire cross section is made of facets, and the

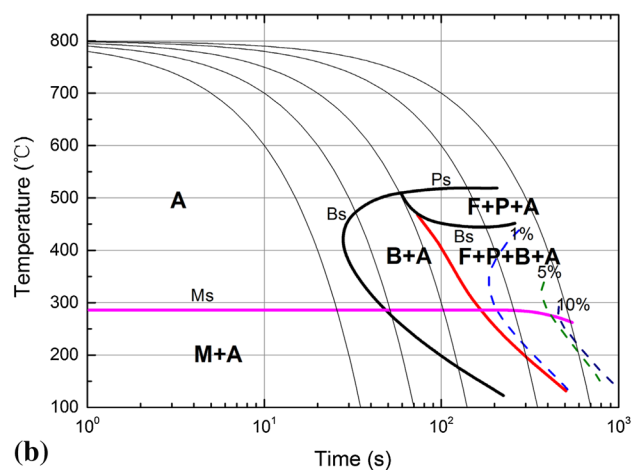


Fig. 3 TTT (a) and CCT (b) graphs of 30CrNi3Mo steel

boundary between the crest and root is distinct due to the plane reflection principle.

The curve of every thread edge can be obtained and is plotted in Fig. 7. It shows the shape change of tooth after tempering process. Compared with the horizontal dimension, the distortion along vertical direction is very tiny. Therefore, the vertical dimension is zoomed into view.

It is found that the straight boundary becomes a periodic wave after the heat treatment in Fig. 7. The amplitude of waves (Δh) is defined as the wavy distortion, and the top cycle is defined as the starting position.

The distortion value of each wavy thread is shown in Fig. 8. There are eleven thread cycles in the component totally. The distortions of first seven cycles were measured. It is found that the distortion decreases with the cycle number. The distortion of all other cycles were barely detectable as small deformation. As the tolerance of distortion is 5 μm , in precise assembly for this component, it is difficult to assemble the screw nut to threaded rod due to the large distortion. The result is more consistent with practical production.

3. Modeling the Quenching-Tempering Process

In the quenching process, hot components are cooled to room temperature by immersing into liquid and spraying or pouring.

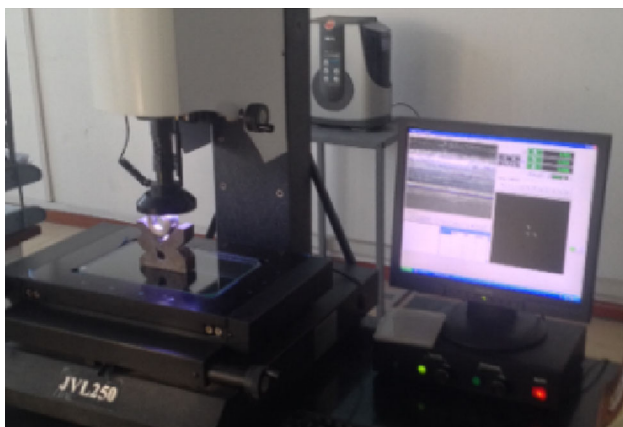


Fig. 4 Video measuring system used

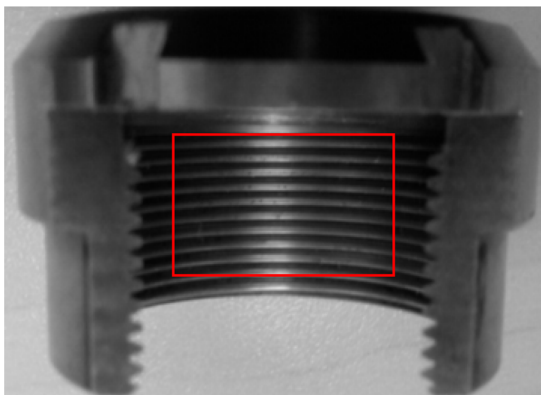


Fig. 5 Split component and image of the thread tooth. The region within red rectangle is the observation region

Today, immersion quenching is the most widely used technique, aiming for martensitic and bainitic hardening of steel. The quenching medium can be water, oil, or an aqueous polymer solution (Ref 15).

3.1 Intercoupling Physical Fields in Heat Treatment

Heat treatment contains three intercoupling physical fields that are shown in Fig. 9. The main physical fields are the temperature field, stress/strain field, and microstructure field.

First, temperature is the fundamental factor that influences the entire heat treatment process. Heat transfers from the surface to the interior, and then thermal gradients generate stress and strain in the component being treated. The changing temperature of the component is the primary driving force of phase transformations, resulting in a change in the microstructure. Furthermore, stress can induce or inhibit phase transformations because it can influence the transformation kinetics. When the material emerges, it has suffered considerable deformation and can induce heat, but this heat is usually ignored in mathematical calculations. Finally, latent heat is released during the phase transformation, which can affect the thermal field. Transformation-induced plasticity (TRIP) phenomenon can also occur during the phase transformation process (Ref 16-19).

3.2 Transformation Kinetics

Numerous kinetic equations have been proposed to describe the phase transformation process. The Johnson-Mehl-Avrami-

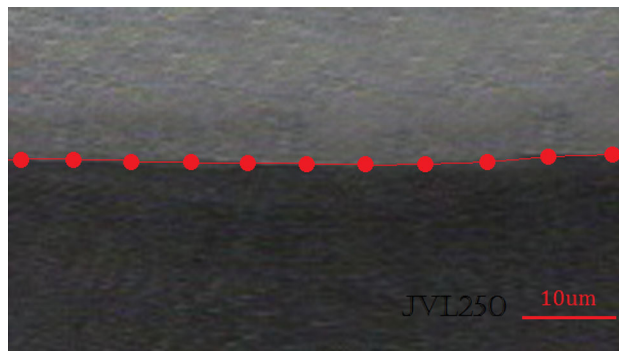
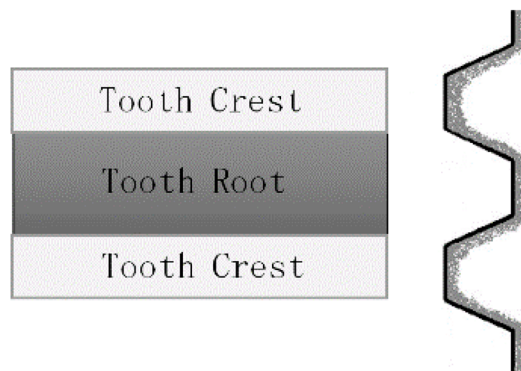


Fig. 6 The thread boundary of tooth root and crest obtained by video measuring system. The bright part is tooth crest, the black part is tooth root, and then boundary is red line



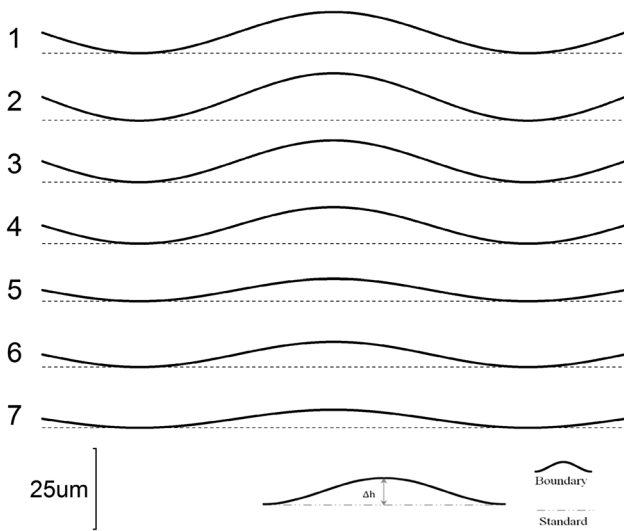


Fig. 7 Schematic of the thread boundary shape. The vertical dimension is zoomed into view

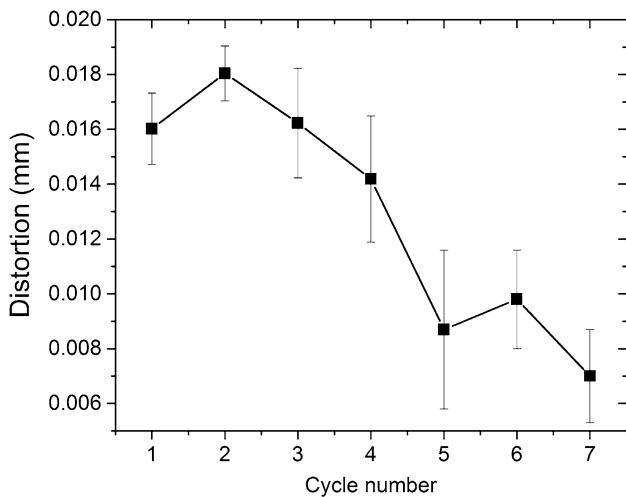


Fig. 8 The distortion of each wavy thread

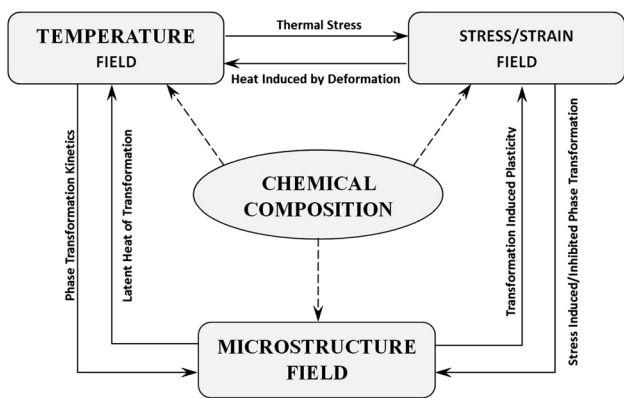


Fig. 9 Physical fields and intercoupling in the heat treatment process

Kolmogorov equation describes how solids transform from one phase into another at a constant temperature (Ref 20-22). The Koistinen-Marburger equation is widely used to describe

Table 2 Parameters used in the transformation kinetics

Austenite to pearlite	$\alpha_1 = 0.8103$	$\beta_1 = 0.8138$
Austenite to ferrite	$\alpha_1 = 0.2243$	$\beta_1 = -0.0722$
Austenite to bainite	$\alpha_1 = 0.7188$	$\beta_1 = -0.1674$
Austenite to martensite	$\alpha_2 = 0.7102$	$\beta_2 = 0.8995$

martensite transformation kinetics, especially for low-alloy steel (Ref 23).

During the quenching process, different areas experience different cooling rates, and both diffusive and non-diffusive transformations will occur. The diffusive and non-diffusive transformation models are used to describe the kinetics of the transformation in Eq 1 and 2 (Ref 20-23):

$$\frac{d\Psi_d}{dt} = f_d(T)\Psi_d^{\alpha_1}(1 - \Psi_d)^{\beta_1}\Psi_a, \quad (\text{Eq 1})$$

$$\frac{d\Psi_n}{dT} = f_n \cdot (1 - \Psi_n)^{\alpha_2}(\Psi_n + \psi\Psi_d)^{\beta_2}\Psi_a, \quad (\text{Eq 2})$$

where Ψ_d is the volume fraction of the diffusive phase, including pearlite and bainite; Ψ_n is the volume fraction of the martensite phase; Ψ_a is the volume fraction of austenite; $f_d(T)$ is a dynamic temperature function; α_1 and β_1 are the constants of diffusive transformation; f_n is a dynamic constant parameter; and α_2 and β_2 are the constants of the non-diffusive transformation. As shown in Table 2, all of the parameters in transformation kinetics are fitted by CCT diagram.

The transformation kinetics during the tempering process can be described as follows (Ref 24):

$$\lambda = \ln \tau - \frac{Q}{2.3RT} + \ln A, \quad (\text{Eq 3})$$

$$\xi = 1 - \exp\left[-5\left(\frac{\lambda - \lambda_0}{\lambda_1 - \lambda_0}\right)^3\right], \quad (\text{Eq 4})$$

where τ is the time of heat preservation, Q is the active energy, R is the gas constant, A is a constant, and T is the absolute temperature. In addition, λ is an intermediate variable, λ_0 and λ_1 are dependent on the transformation type, and ξ is the amount of tempered martensite. For tempering process in 30CrNi3Mo steel, $Q = 418.68$ kJ/mol, $\ln A = 50$, $\lambda_0 = 0.5$, and $\lambda_1 = 25.3$ (Ref 25).

3.3 Heat Boundary Conditions

The heat conduction equation that determines the temperature fields is given as follows:

$$\rho c \dot{T} - \nabla \cdot (k \nabla T) - r = 0, \quad (\text{Eq 5})$$

where ρ is the density, c is the specific heat, r is the internal heat source, and k is the heat conductivity. The heat conductivities of all phases in 30CrNi3Mo steel are measured by FLA (laser flash diffusivity apparatus) in Table 3.

Heat convection is the transfer of heat from one place to another by the movement of fluids. This transfer is called mass transfer. Convection cooling is sometimes called “Newton’s law of cooling” when the heat transfer coefficient is indepen-

dent or relatively independent of the temperature difference between the object and the environment.

$$q_x = h(T_o - T_e), \quad (\text{Eq 6})$$

where q_x is the heat flux density, h is the heat transfer coefficient (HTC), T_o is the temperature of the object surface, and T_e is the temperature of the environment. The HTC of the quenchant can be measured experimentally (Ref 26, 27).

Thermal radiation is also considered in the simulation. Thermal radiation is electromagnetic radiation that is generated by the thermal motion of charged particles in matter. All matter with a temperature greater than absolute zero emits thermal radiation. The Stefan-Boltzmann law is used to describe the heat flux density in thermal radiation from the object to the environment.

$$q_x = \varepsilon\sigma(T_o^4 - T_e^4), \quad (\text{Eq 7})$$

where ε is the emissivity factor, σ is the Stefan-Boltzmann constant, T_o is the temperature on the object surface, and T_e is the temperature of the environment. In the simulation, $\varepsilon = 0.75$ and $\sigma = 5.670373 \times 10^{-8} \text{W/m}^2 \cdot \text{K}^4$ were used.

Table 3 Heat conductivity of 30CrNi3Mo steel

Phase	Thermal conductivity (J/m · K)
Austenite	$16 + 1.30 \times 10^{-2} \times (T - 293)$
Ferrite	$59 - 2.25 \times 10^{-2} \times (T - 293)$
Pearlite	$43 - 1.90 \times 10^{-2} \times (T - 293)$
Bainite	$16 + 1.30 \times 10^{-2} \times (T - 293)$
Martensite	$25 + 3.00 \times 10^{-3} \times (T - 293)$
Tempered martensite	$25 + 3.00 \times 10^{-3} \times (T - 293)$

3.4 Mechanical Model

For the mechanical model, the small deformation theory was used where the total strain, ε , can be additively decomposed into five components (Ref 11):

$$\varepsilon = \frac{1}{2} [\nabla \bar{u} + (\nabla \bar{u})^T] = \varepsilon^e + \varepsilon^p + \varepsilon^{\text{th}} + \varepsilon^{\text{tr}} + \varepsilon^{\text{tp}}, \quad (\text{Eq 8})$$

where ε^e is the elastic strain, ε^p is the plastic strain, ε^{th} is the strain of the thermal effect, ε^{tr} is the strain of the phase transformation, and ε^{tp} is the strain of the TRIP.

Greenwood and Johnson (Ref 28) observed phase transformation plasticity under low stress that changed the stress distribution due to an orientation effect. Phase transformation plasticity is the irreversible deformation generated when a phase transformation occurs under stress, for which the equivalent stress is lower than the yield strength of the material (Ref 29). The transformation plasticity strain can be described by the following equation (Ref 30-33):

$$\varepsilon_{ij}^{\text{tp}} = K\sigma_{ij}f(\xi), \quad (\text{Eq 9})$$

where $\varepsilon_{ij}^{\text{tp}}$ is the transformation plasticity strain, $K = 9.4 \times 10^{-5}$ is the transformation plasticity coefficient, σ_{ij} is the external stress, ξ is the fraction that undergoes a phase transformation, and $f(\xi) = \xi(2 - \xi)$ is the kinetics of the transformation plasticity.

4. Simulation Validation

DANTE was used to simulate the entire heat treatment process for the temperature field and distortion field. DANTE

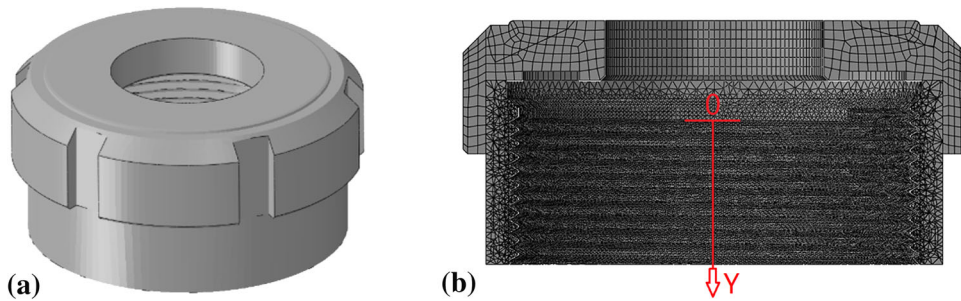


Fig. 10 Geometry (a) and finite element mesh (b) in cut open view

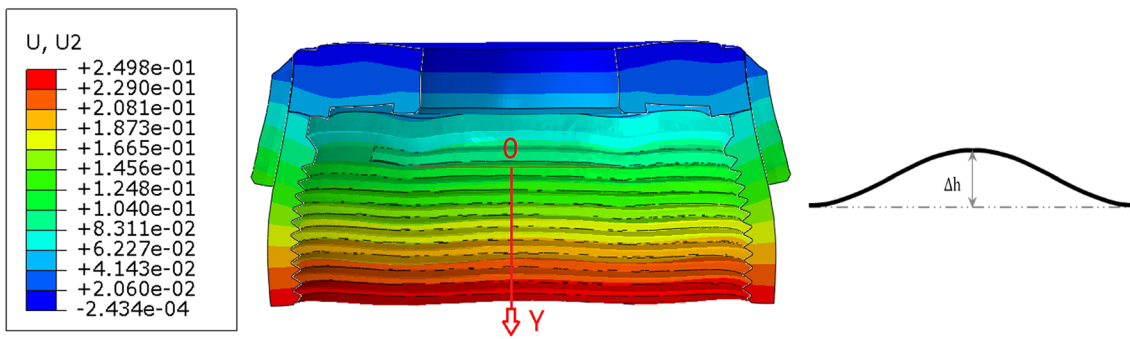


Fig. 11 Wavy distortions after tempering process, tempered for 1.5 h at 200 °C. U2 is the distortion along Y direction

subroutines combine mechanical models, metallurgical phase transformation models, and mass diffusion models that couple with ABAQUS/STD's diffusion, thermal and stress/displacement (static) solvers to calculate a steel component's response to a heat treatment process. Distortion of the internal threads is measured using a semi-destructive testing method. In addition, the microstructure of the component was analyzed using XRD. It was found that the FEA model can accurately predict the distortion and microstructure field throughout the quenching-tempering process.

4.1 The Finite Element Model

The geometry of the precision screw nut in this study is shown in Fig. 10. Due to the existence of the inner thread, the screw nut cannot be treated as periodic symmetry. The whole part is meshed for analysis. The model has 77147 nodes, 16973 linear hexahedral elements of type C3D8R, and 255690 linear tetrahedral elements of type C3D4.

4.2 Validation of the FEA Model

Numerical simulation is conducted with all parameters same as the experiment. The distortion along Y direction after tempering is presented in Fig. 11. After the heat treatment, the

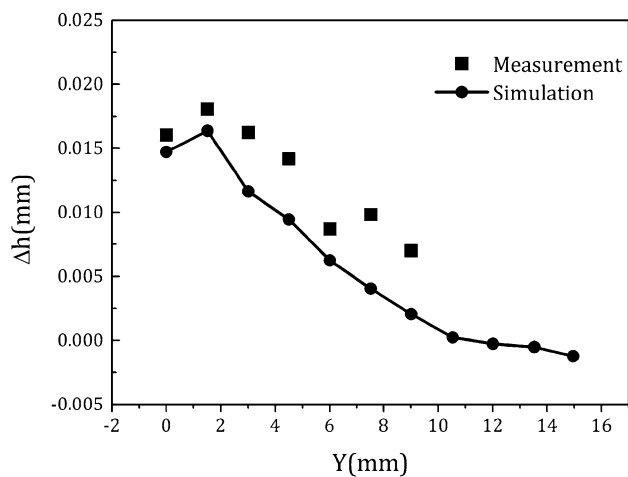


Fig. 12 Validation of distortion values by simulation and measurement. (a) Pearlite, (b) martensite, and (c) tempered martensite

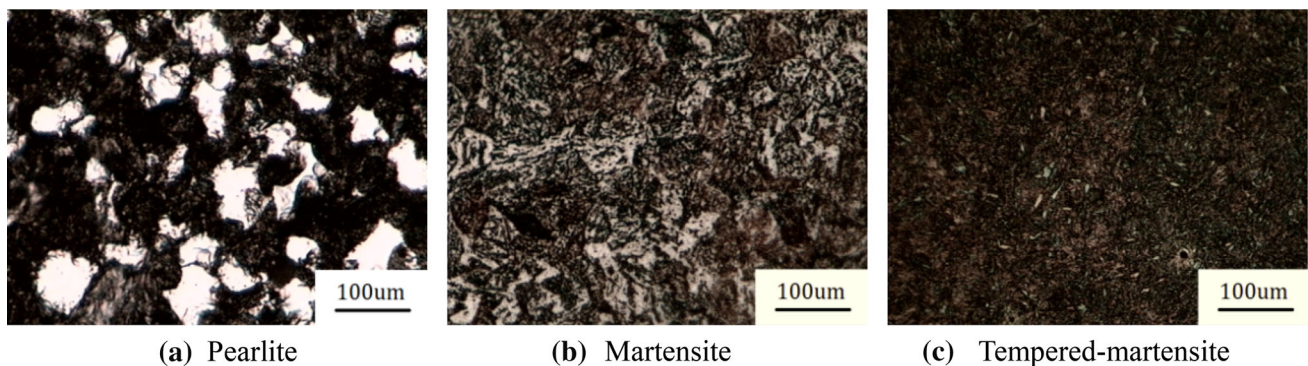


Fig. 13 Metallographs of the 30CrNi3Mo steel in different microstructure states. (a) Austenite (wt.%), (b) martensite (wt.%), and (c) tempered martensite (wt.%)

shape of the internal thread changes from straight lines to periodic waves in current view plane.

In Fig. 12, the fold line is the simulated value and the rectangular scattered points are the measured values. The average error between the experimental and modeled data is <20%.

The existence of the thick cap with six grooves induces a huge temperature gradient, which then induces a larger distortion. The distortion of the internal threads gradually increases from the bottom to the top. The maximum distortion occurs in the second cycle rather than in the first cycle. The stress is concentrated at the junction between the thick wall and the thin wall, where the maximum thermal stress occurs. Due to a high stiffness at the top end, the first cycle thread may be restricted.

4.3 Validation of the Microstructure Fields

30CrNi3Mo steel has an excellent hardenability. The initial microstructure before quenching and tempering is pearlite. After the quenching process, the microstructure is consistent with mass lath martensite and little austenite is retained. Then, the martensite is transformed into tempered martensite during the tempering process. The metallographs of the three microstructures are shown in Fig. 13.

The simulation results of microstructure after tempering are shown in Fig. 14. It can be seen that the martensite and tempered martensite are the main microstructures. As the tempering temperature is only 200 °C, and the holding time is only 1.5 h, almost 95% martensite was preserved. Martensite can enhance the hardness and wear resistance of the threads.

XRD analysis is used to test the volume of retained austenite in steel. The XRD pattern of the material in the black rectangle in Fig. 14a is shown in Fig. 15. The volume fraction of the retained austenite can be calculated as follows (Ref 34):

$$V_A = \frac{I_A/R_A}{I_A/R_A + I_M/R_M}, \quad (\text{Eq } 10)$$

where V_A is the volume fraction of austenite, I is the diffraction peak intensity, and the R -value is calculated according to a previously reported method (Ref 34). From the XRD pattern, it is found that the retained austenite accounts for approximately 2% after tempering. It agrees well with the simulation result.

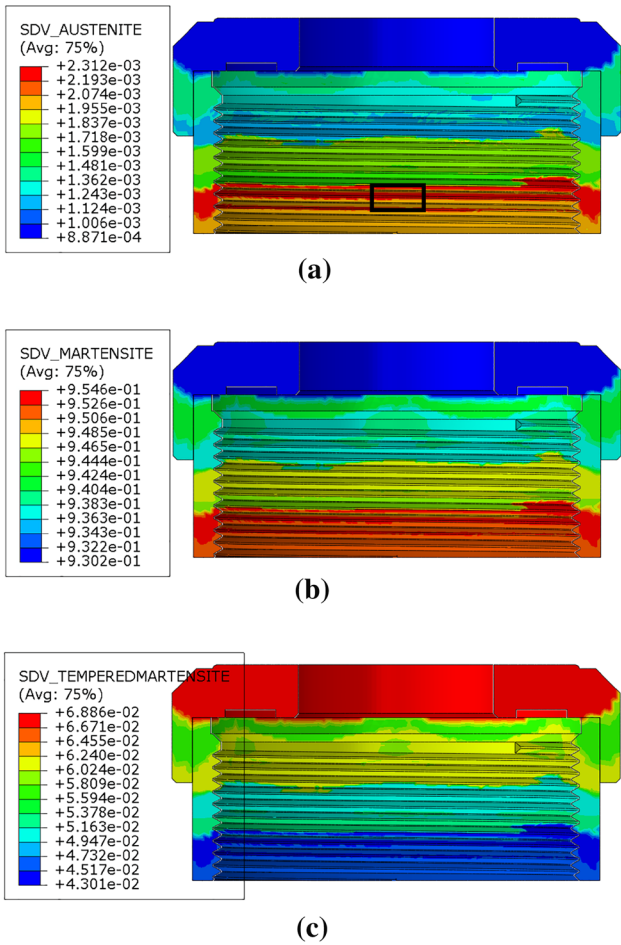


Fig. 14 Microstructure fields after tempering process. Material within the black rectangle is for XRD analysis, Unit: 100%. (a) Austenite (wt.%), (b) martensite (wt.%), (c) tempered martensite (wt.%)

4.4 Validation of Hardness

Material hardness of the last thread is measured to validate the simulation model. In Fig. 16, the holding time is 2 h and the tempering temperature is varied from 100 to 250 °C. The Rockwell hardness of the threads is used to measure this quenching-tempering state. The simulated and experimental results are shown together for comparison. The hardness is observed to decrease with temperature. It can be seen that the simulation hardness agrees well with the experimental results.

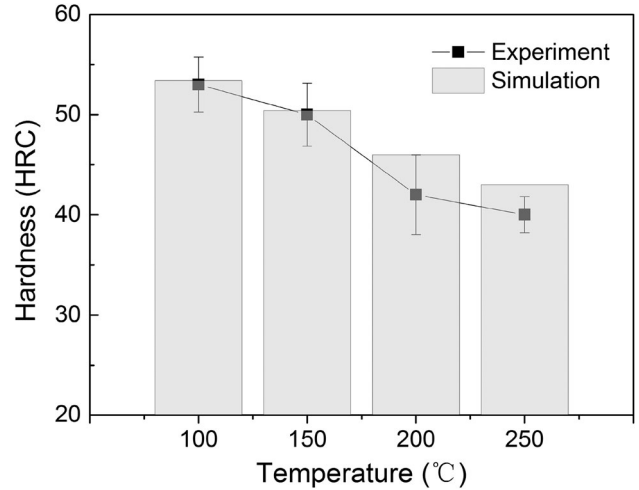


Fig. 16 Hardness values by both experiment and simulation (tempering for 2 h). (a) Hardness, (b) rate of hardness change, (c) residual stress, and (d) rate of residual stress change

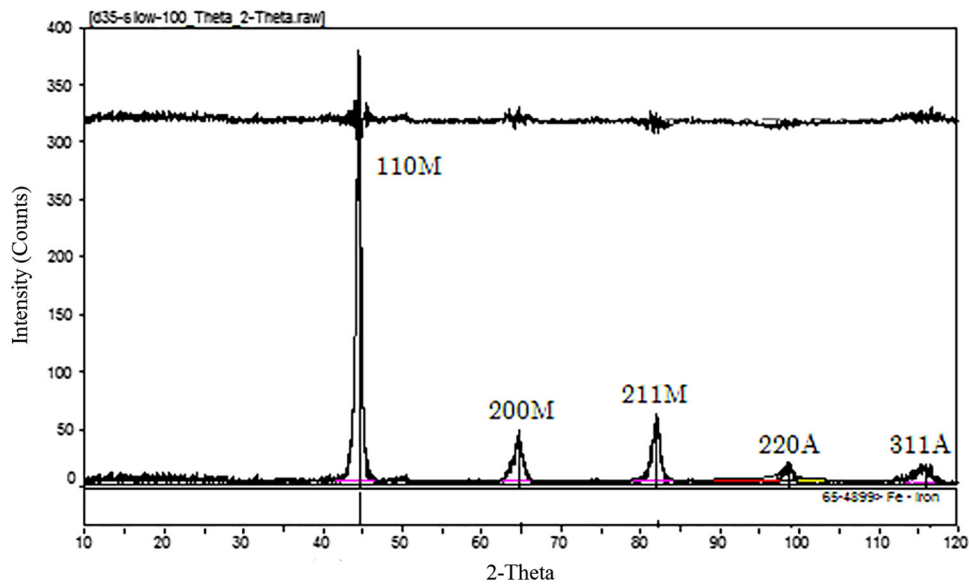


Fig. 15 XRD pattern of the steel. The retained austenite accounts for approximately 2% after tempering

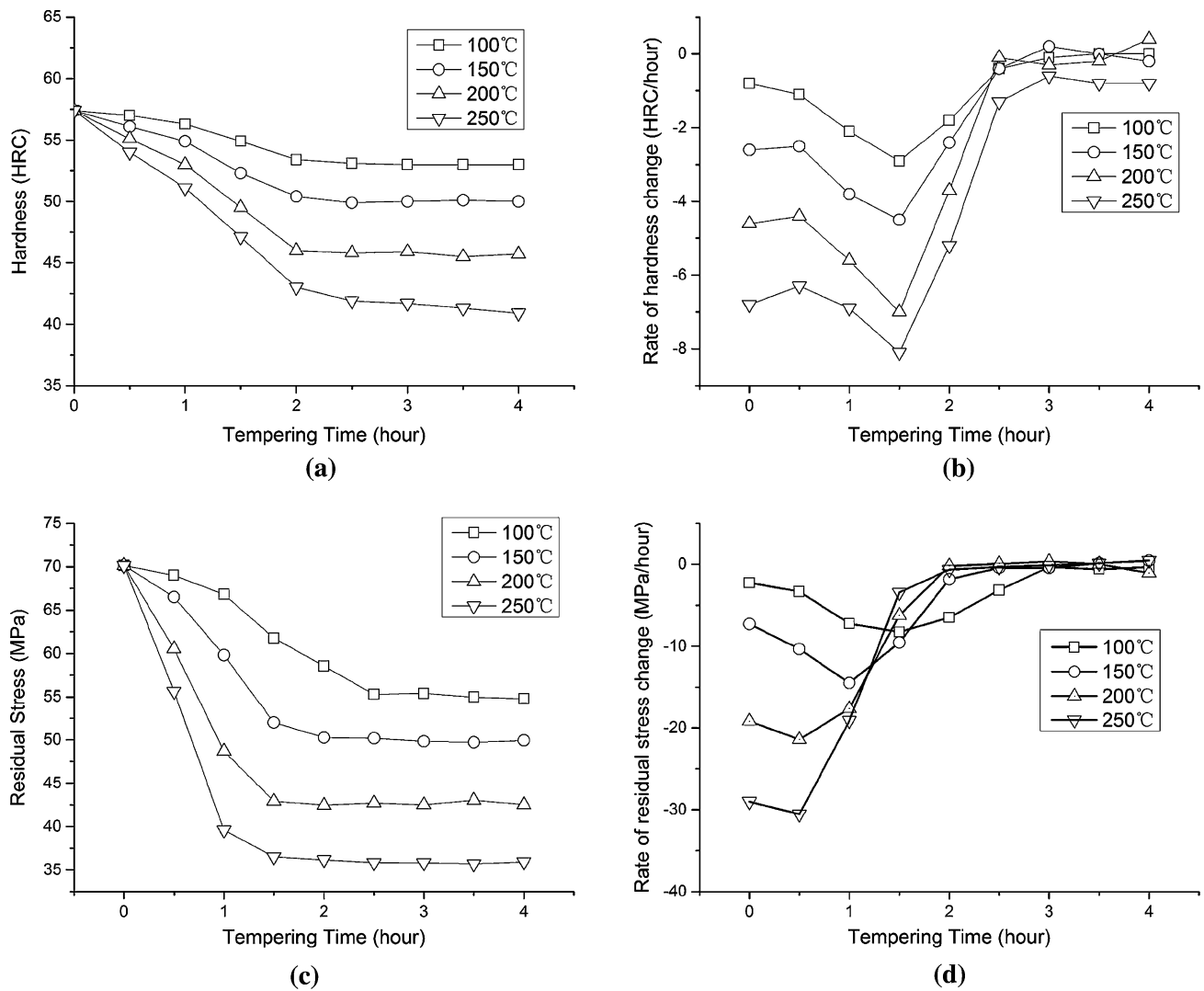


Fig. 17 Hardness and residual stress changes in tempering process by simulation. (a) Hardness, (b) rate of hardness change, (c) residual stress, (d) rate of residual stress change

5. Discussion

In this section, the effects of various parameters (tempering temperature and holding time) in the tempering process, different quenchants (UCON, water, and oil), immersion orientation, air transfer, and simulation without grooves are explored. It was found that the conditions used significantly influence the distortion and residual stress in the quenching-tempering process.

5.1 Effects of the Parameters in Tempering

In the tempering process simulation, all of the parameters in the quenching step were held constant, and the tempering temperature and holding time were varied within certain limits. The simulation explored tempering temperatures ranging from 100 to 250 °C in increments of 50 °C and holding times from 0 to 3 h in 0.5-h increments.

The variation in hardness of the last thread at different holding times and temperatures is shown in Fig. 17a. At lower temperatures, the hardness remains almost unchanged with

time. However, the hardness decreases sharply at a higher temperature, corresponding to the transformation of martensite to tempered martensite under these conditions. The rate at which the hardness varies is shown in Fig. 17b. The rate decreases with time and increases with temperature.

The residual stress of threads is presented in Fig. 17c. The residual stress decreases with time, dropping off sharply and rapidly at high tempering temperatures. The rate of residual stress change decreases with time and increases with temperature, as shown in Fig. 17d.

Both the hardness and residual stress decrease with increasing temperature and time. The average rate of descent in the phase transformation period has a positive relationship with temperature, as shown in Fig. 18. This relationship indicates that both the hardness and residual stress behave similarly to the kinetics of the tempering process.

5.2 Effect of Quenchants

The heat transfer coefficients of three quenchants are shown in Fig. 19. The coefficient of quenching oil is embedded in

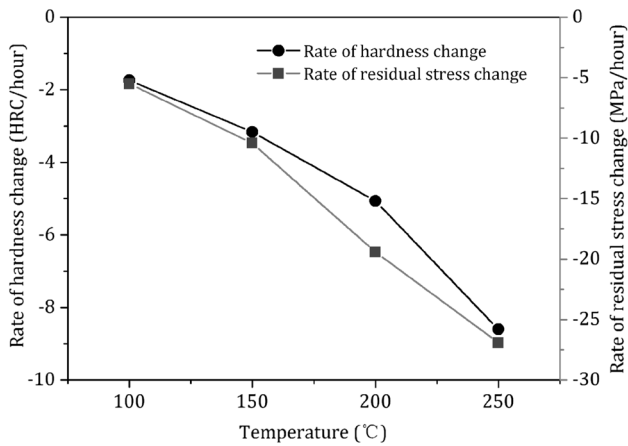


Fig. 18 Average rates of hardness and residual stress change versus temperature by simulation

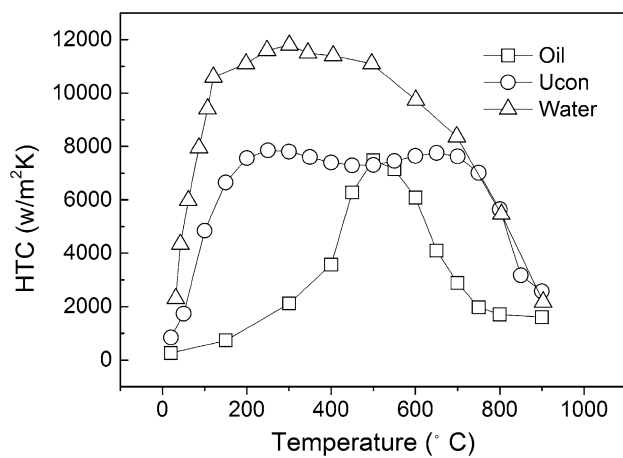


Fig. 19 Heat transfer coefficient of different quenchants with temperature. (a) Oil (current condition), (b) UCON, and (c) water

Dante, and the other two are measured by experiments (Ref 35). The distortions after tempering are calculated and shown in Fig. 20, and the maximal residual stress and distortion are shown in Fig. 21.

It is clear that the current quenchant (Oil) is the best choice with the smallest residual stress and distortion. Water will induce large distortions and huge residual stress after heat treatment due to its high cooling capacity at low temperatures. While UCON is usually used as the quenchant in the aluminum alloy quenching process, it is not suitable for 30CrNi3Mo steel due to its high cooling ability at high temperatures.

5.3 Effect of Immersion Orientation

The small end was immersed into water first in this experiment and simulation. The reverse orientation was then considered by simulation. That is, the large end with six grooves was immersed into the quenchant first.

From Fig. 22, the distortion observed for the reversed orientation is smaller than the initial distortion. This phe-

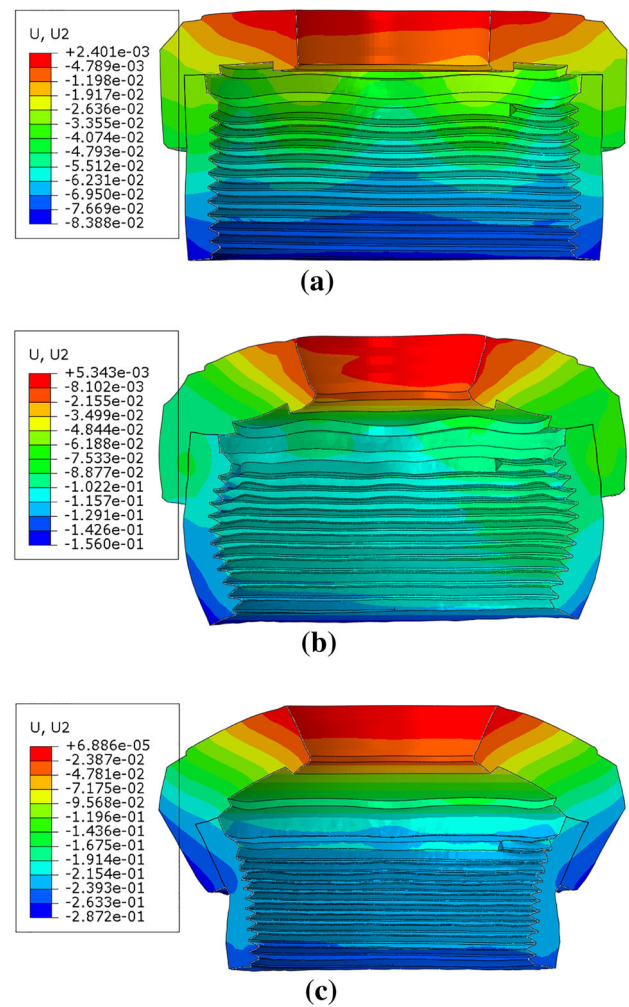


Fig. 20 Distortions under different quenchants (all magnified by 50 times), unit: mm. (a) Oil (current condition), (b) UCON, and (c) water

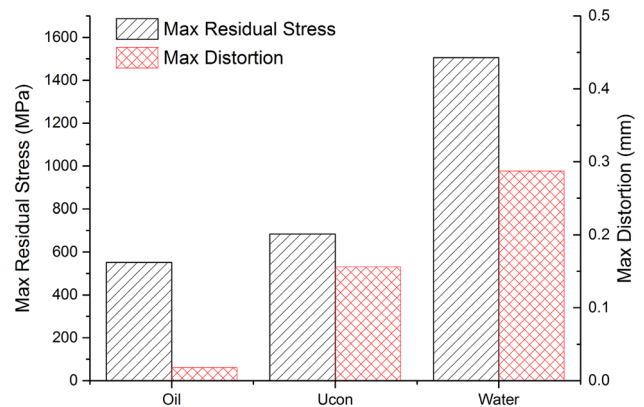


Fig. 21 Maximal residual stress and distortion under different quenchants

nomenon can be observed in industrial manufacturing named orientation effect (Ref 36). The large end prior to immersion is suggested because of smaller distortion.

5.4 Effect of Air Transfer and Immersion Steps on the Simulation

The air transfer process and immersion process are usually ignored in simulations. However, these two steps are part of the real heat treatment process and affect the distortion significantly. Simulations without air transfer and without immersion were carried out separately.

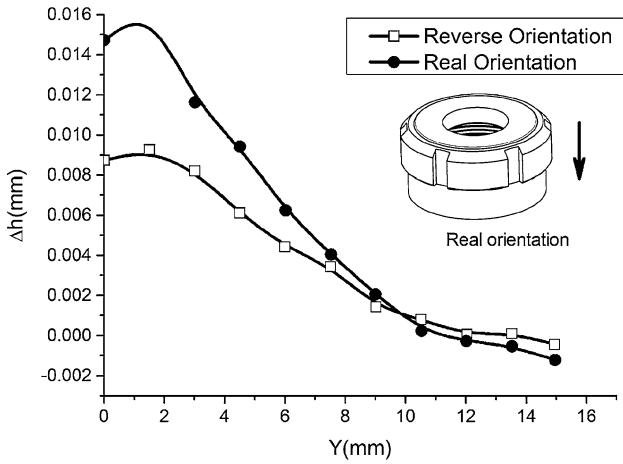


Fig. 22 Distortions under different immersion orientations by simulation

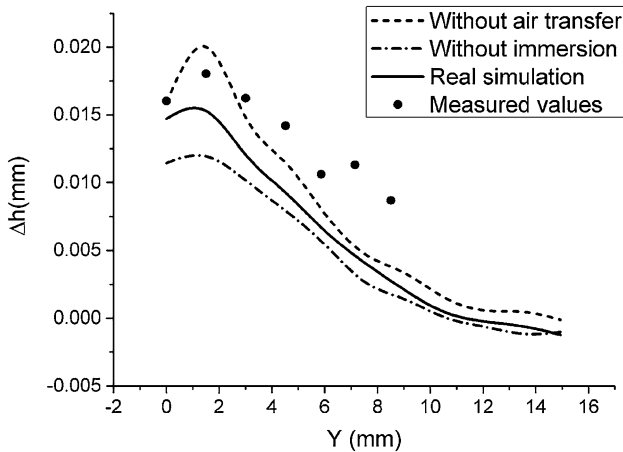


Fig. 23 Distortion under three presumed conditions by simulation: (a) with grooves and (b) without grooves

Figure 23 shows the respective distortions without the air transfer and immersion steps resulting from numerical simulations. Compared with the distortion in real process simulations, the distortion is greater in the simulations without the air transfer process and smaller in simulations without the immersion process. All distortion curves exhibit the same variation trend along the axial direction.

Air transfer reduces the surface temperature of the component and relieves the temperature gradient in the quenching process. Thus, the residual stress can be slightly smaller when air transfer is used.

In the immersion process, the small end is first immersed into the quenchant. The temperature difference between the large and small ends is larger after immersion. It is important to consider both the air transfer and immersion processes in the simulation during heat treatment.

5.5 Effect of Grooves on Distortions

The grooves are machined before heat treatment in the current manufacturing process. The waved distortions of the internal threads have the same phase positions as the six outer grooves, and this phenomenon can be easily observed in Fig. 24. The heat treatment simulation of the component without grooves was also carried out. The results show that there are no waved distortions in the internal thread without grooves as shown in Fig. 25. The residual stress in the internal threads is < 180 MPa.

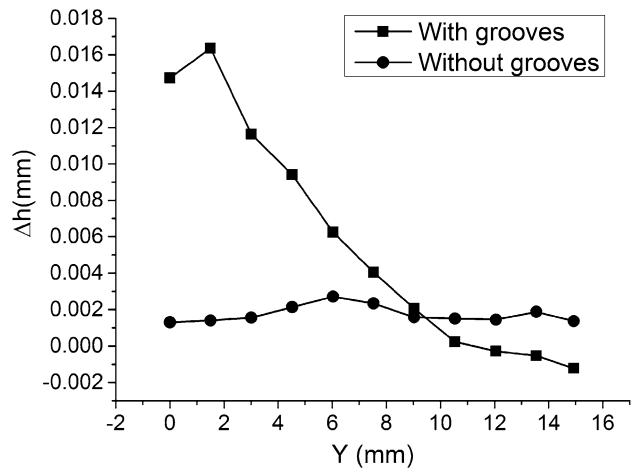


Fig. 25 Thread distortions along the vertical orientation by simulation

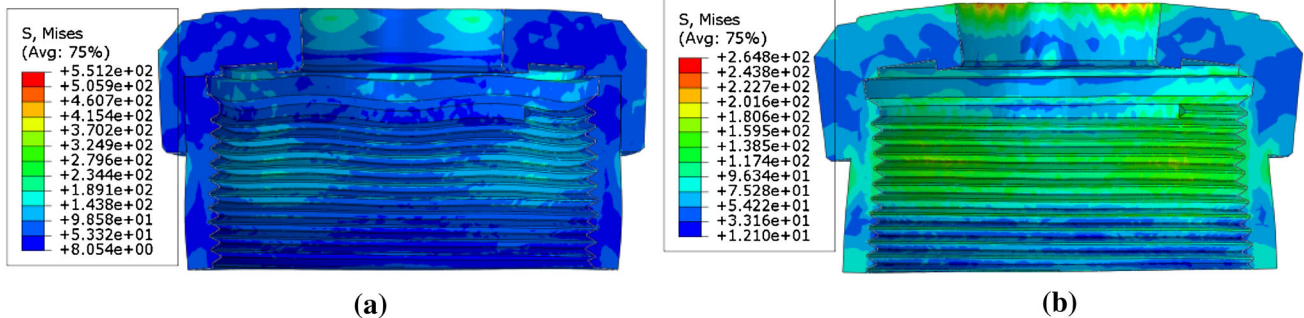


Fig. 24 Distortion and stress fields after tempering (distortion is magnified by 50 times). (a) With grooves, (b) without grooves

The grooves can cause inconsistencies in the thermal field in the flange, resulting in large residual stress and distortions. As a result, grooves should be machined after heat treatment if permitted.

6. Conclusions

A medium-carbon low-alloy steel precision component with internal threads was quenched and tempered at low temperatures. The distortion of the internal threads results in subsequent assembly difficulties. The distortion of the internal thread was measured using a video measuring system, which is a semi-destructive technique. It was found that this measurement method can capture the micro-distortion of the internal thread effectively. Numerical simulation of the entire quenching-tempering process was conducted. The FEA model used was validated by the precision measurement results and hardness change.

Periodic wavy distortions of the internal thread occur after heat treatment. The wavy distortion is relatively bigger near the top end and then decreases from the top to the bottom. The maximum distortion occurs in the second cycle and not in the first. This results from the high stiffness of the top end.

Different tempering temperatures and heat holding times were used in orthogonal simulation testing. The simulation results of the hardness and residual stress after the tempering process agreed with the experimental data. Both the hardness and residual stress decrease with increasing temperature and time. The rate of descent has a positive relationship with temperature.

Three different quenchants were investigated through simulations, and the results indicate that oil is the best choice, exhibiting the lowest distortion. Water will induce large distortions and huge residual stress after the heat treatment due to its high cooling capacity at low temperatures. UCON, a quenchant usually used in the aluminum alloy quenching process, is not suitable for 30CrNi3Mo steel due to its high cooling ability at high temperatures.

Two immersion orientations were compared in the simulation. The results indicate that the distortion is smaller when the larger end is immersed first. Simulations without the air transfer step and without the immersion step were conducted separately. The simulation accounting for air transfer and immersion steps conforms to the measured values better than the simulations that do not consider both of these steps. Therefore, it is important to consider both the air transfer and immersion steps of the heat treatment in simulations.

A simulation without grooves was conducted, and the results show that there are no wavy distortions in the internal thread without grooves. The maximum residual stress is < 180 MPa. The grooves cause inconsistencies in the thermal field, which result in larger distortions. Therefore, grooves should be machined after heat treatment if conditions permit.

Acknowledgments

This research has been financially supported by the National Basic Research Program of China (2011CB013404) and the National Natural Science Foundation of China (51275254). This research was supported by Tsinghua National Laboratory for Information Science and Technology.

References

1. C. Şimşir and C.H. Gür, 3d FEM Simulation of Steel Quenching and Investigation of the Effect of Asymmetric Geometry on Residual Stress Distribution, *J. Mater. Process. Technol.*, 2008, **207**(1-3), p 211–221
2. K.O. Lee et al., A Study on the Mechanical Properties for Developing a Computer Simulation Model for Heat Treatment Process, *J. Mater. Process. Technol.*, 2007, **182**(1-3), p 65–72
3. Z. Li et al., Modeling the Effect of Carburization and Quenching on the Development of Residual Stresses and Bending Fatigue Resistance of Steel Gears, *J. Mater. Eng. Perform.*, 2013, **22**(3), p 664–672
4. M. Reich, Numerical and Experimental Analysis of Residual Stresses and Distortion in Different Quenching Processes of Aluminum Alloy Profiles, *6th International Conference on Quenching and Control of Distortion*, ASM, 2012
5. V. Nemkov et al., Stress and Distortion Evolution During Induction Case Hardening of Tube, *J. Mater. Eng. Perform.*, 2013, **22**(7), p 1826–1832
6. A.D. da Silva et al., Distortion in quenching an Aisi 4140 C-Ring: Predictions and Experiments, *J. Mater. Des.*, 2012, **42**, p 55–61
7. E. Brinksmeier et al., Distortion Minimization of Disks for Gear Manufacture, *Int. J. Mach. Tools Manuf.*, 2011, **51**(4), p 331–338
8. S.-J. Lee and Y.-K. Lee, Finite Element Simulation of Quench Distortion in a Low-Alloy Steel Incorporating Transformation Kinetics, *J. Acta Mater.*, 2008, **56**(7), p 1482–1490
9. A. Yamanaka, T. Takaki, and Y. Tomita, Elastoplastic Phase-Field Simulation of Martensitic Transformation with Plastic Deformation in Polycrystal, *Int. J. Mech. Sci.*, 2010, **52**(2), p 245–250
10. C.M. Amey, H. Huang, and P.E.J. Rivera-Diaz-del-Castillo, Distortion in 100cr6 and Nanostructured Bainite, *J. Mater. Des.*, 2012, **35**, p 66–71
11. A.K. Nallathambi et al., Sensitivity of Material Properties on Distortion and Residual Stresses During Metal Quenching Processes, *J. Mater. Process. Technol.*, 2010, **210**(2), p 204–211
12. B. Smoljan, Prediction of Mechanical Properties and Microstructure Distribution of Quenched and Tempered Steel Shaft, *J. Mater. Process. Technol.*, 2006, **175**(1), p 393–397
13. C. Liu, X. Xu, and Z. Liu, A FEM Modeling of Quenching and Tempering and Its Application in Industrial Engineering, *J. Finite Elem. Anal. Des.*, 2003, **39**(11), p 1053–1070
14. D.-H. Huang and G. Thomas, Structure and Mechanical Properties of Tempered Martensite and Lower Bainite in Fe-Ni-Mn-C Steels, *J. Metall. Trans.*, 1971, **2**(6), p 1587–1598
15. J. Mackerle, Finite Element Analysis and Simulation of Quenching and Other Heat Treatment Processes: A Bibliography (1976-2001), *J. Comput. Mater. Sci.*, 2003, **27**(3), p 313–332
16. F.D. Fischer and S.M. Schlogl, The Influence of Material Anisotropy on Transformation Induced Plasticity in Steel Subject to Martensitic Transformation, *J. Mech. Mater.*, 1995, **21**(1), p 1–23
17. P.J. Jacques et al., Multiscale Mechanics of Trip-Assisted Multiphase Steels: I. Characterization and Mechanical Testing, *J. Acta Mater.*, 2007, **55**(11), p 3681–3693
18. H.N. Han and D.-W. Suh, A Model for Transformation Plasticity During Bainite Transformation of Steel under External Stress, *J. Acta Mater.*, 2003, **51**(16), p 4907–4917
19. M.-G. Lee, S.-J. Kim, and H.N. Han, Finite Element Investigations for the Role of Transformation Plasticity on Springback in Hot Press Forming Process, *J. Comput. Mater. Sci.*, 2009, **47**(2), p 556–567
20. M. Avrami, Kinetics of Phase Change. I, General Theory, *J. Chem. Phys.*, 1939, **7**, p 1103–1112
21. M. Avrami, Kinetics of Phase Change. Ii Transformation-Time Relations for Random Distribution of Nuclei, *J. Chem. Phys.*, 1940, **8**(2), p 212
22. M. Avrami, Granulation, Phase Change, and Microstructure Kinetics of Phase Change. Iii, *J. Chem. Phys.*, 1941, **9**(2), p 177
23. D.P. Koistinen and R.E. Marburger, A General Equation Prescribing the Extent of the Austenite-Martensite Transformation in Pure Iron-Carbon Alloys and Plain Carbon Steels, *J. Acta Metall.*, 1959, **7**(1), p 59–60
24. K. Inoue, Study About Tempering Process, *Tetsu-To-Hagane*, 1982, **00**, p 25–30
25. W. Shi et al., Experimental Study of Microstructure Evolution During Tempering of Quenched Steel and Its Application, *J. Trans. Mater. Heat Treat.*, 2004, **25**, p 736–739
26. H. Kim and S. Oh, Evaluation of Heat Transfer Coefficient During Heat Treatment by Inverse Analysis, *J. Mater. Process. Technol.*, 2001, **112**(2), p 157–165

27. R. Price and A. Fletcher, Determination of Surface Heat-Transfer Coefficients During Quenching of Steel Plates, *J. Met. Technol.*, 1980, **7**(1), p 203–211
28. G.W. Greenwood and R.H. Johnson, The Deformation of Metals under Small Stresses During Phase Transformations, *Proc. R. Soc. Lond. Ser. A (Math. Phys. Sci.)*, 1965, **293**(1394), p 403–422
29. W. Shi and Z. Nie, Experiment and Modeling of Stress Affected Bainitic Transformation, *Proceedings of The 20th Congress of International Federation for Heat Treatment and Surface Engineering*, Beijing, 2012, p 864–867
30. B. Verlinden et al., Austenite Texture and Bainite/Austenite Orientation Relationships in Trip Steel, *J. Scr. Mater.*, 2001, **45**(8), p 909–916
31. N. Tsuchida and Y. Tomota, A Micromechanic Modeling for Transformation Induced Plasticity in Steels, *J. Mater. Sci. Eng. A*, 2000, **285**(1), p 346–352
32. F. Fischer et al., A New View on Transformation Induced Plasticity (Trip), *Int. J. Plast.*, 2000, **16**(7), p 723–748
33. F. Fischer, Q.-P. Sun, and K. Tanaka, Transformation-Induced Plasticity (Trip), *J. Appl. Mech. Rev.*, 1996, **49**(6), p 317–364
34. ASTM, Standard Practice for X-Ray Determination of Retained Austenite in Steel with near Random Crystallographic Orientation, *E975-03*, ASTM, 2013
35. P. Du et al., A FEM-Based Inverse Calculation Method for Determination of Heat Transfer Coefficient in Liquid Quenching Process, *TMS 2014 143rd Annual Meeting & Exhibition, Annual Meeting Supplemental Proceedings*, Wiley, New York, 2014
36. V. Srinivasan et al., Numerical Simulation of Immersion Quenching Process of an Engine Cylinder Head, *J. Appl. Math. Model.*, 2010, **34**(8), p 2111–2128